Cross-satellite calibration of high-energy electron fluxes measured by FengYun-4A based on Arase observations

XiaoYu Wang[1], Xing Cao[1]*, Xin Ma[1]*, XiaoXin Zhang[2,3], AnQin Chen[2,3], JunHu Dong[1], BinBin Ni[1], and XianKang Dou[1]

[1]Department of Space Physics, School of Electronic Information, Wuhan University, Wuhan 430072, China;

[2]Key Laboratory of Space Weather, National Satellite Meteorological Center (National Center for Space Weather), China Meteorological Administration, Beijing 100081, China;

[3]Innovation Center for FengYun Meteorological Satellite (FYSIC), National Satellite Meteorological Center, China Meteorological Administration, Beijing 100081, China

Key Points:

- We conduct an energy-dependent cross-satellite calibration of high-energy electron fluxes measured by FengYun-4A based on Arase observations.
- The cross-satellite calibration factors for 245–894 keV electrons range from 0.67 to 0.81.
- There is better agreement between the electron flux conjunctions after the cross-satellite calibration, as well as much smaller normalized root mean square errors.

Abstract: We use the High-energy Electron Experiments (HEP) instrument onboard Arase (ERG) to conduct an energy-dependent cross-satellite calibration of electron fluxes measured by the High Energy Particle Detector (HEPD) onboard FengYun-4A (FY-4A) spanning from April 1, 2017, to September 30, 2019. By tracing the two-dimensional magnetic positions (*L*, magnetic local time [MLT]) of FY-4A at each time, we compare the datasets of the conjugate electron fluxes over the range of 245–894 keV in 6 energy channels for the satellite pair within different sets of $L \times$ MLT. The variations in the electron fluxes observed by FY-4A generally agree with the Arase measurements, and the percentages of the ratios of electron flux conjunctions within a factor of 2 are larger than 50%. Compared with Arase, FY-4A systematically overestimates electron fluxes at all 6 energy channels, with the corresponding calibration factors ranging from 0.67 to 0.81. After the cross-satellite calibration, the electron flux conjunctions between FY-4A and Arase show better agreement, with much smaller normalized root mean square errors. Our results provide a valuable reference for the application of FY-4A high-energy electron datasets to in-depth investigations of the Earth's radiation belt electron dynamics.

Keywords: cross-satellite calibration; high-energy electron flux; FengYun-4A; Arase

1. Introduction

The energetic electrons in the Earth's radiation belts exhibit a complex and dynamic evolution, owing to an imbalance between the loss and acceleration processes (Horne et al., 2005; Zong QG et al., 2009, 2021; Li LY et al., 2013, 2016a, 2017, 2019; Aseev et al., 2017; Boyd et al., 2018; Xiang Z et al., 2018; Xiong Y et al., 2021; Tang RX et al., 2023). Substorm injection is considered the main source of tens to hundreds of kiloelectron volts (keV) electrons in the Earth's radiation belts (Birn et al., 1997; Li LY et al., 2009; Boakes et al., 2011; Li LY and Wang ZQ, 2018; Nagai et al., 2019; Tang CL et al., 2022; Wang XY et al., 2023). Inward radial diffusion

induced by ultra-low-frequency waves can efficiently accelerate electrons by conserving the first adiabatic invariant (e.g., Miyoshi et al., 2004; Shprits et al., 2008; Su ZP et al., 2015; Zhao H et al., 2019). Various plasma waves, frequently triggered during geomagnetic storms, substorms, or both, play an important role in the acceleration and loss of radiation belt electrons (Cao JB et al., 2013; Xiao FL et al., 2017; Gao ZL et al., 2018; Gu XD et al., 2020; Yue C et al., 2020; Baker, 2021; Yang C et al., 2022; Zhao YW et al., 2022; Ni BB et al., 2023). Chorus waves can locally accelerate tens to hundreds of keV electrons to relativistic energies, resulting in the prominent local peaks of the electron phase space density (PSD) in the radial profile (e.g., Chen Y et al., 2007; Thorne et al., 2013; Li W et al., 2016; Allison and Shprits, 2020). Chorus waves can also scatter energetic electrons into the loss cone, causing radiation belt electrons to precipitate into the atmosphere (Ni BB et al., 2011b; He JB et al., 2021; He Q et al., 2022). Magnetosonic waves can accelerate electrons with ~50°–70° pitch angles via

Landau resonance, forming the butterfly pitch angle distributions over the energy range of ~100 keV to a few megaelectron volts (MeV) (e.g., Horne et al., 2007; Ma QL et al., 2016; Ni BB et al., 2020). In contrast, electromagnetic ion cyclotron (EMIC) waves can cause the local loss of relativistic electrons (e.g., Ni BB et al., 2015, 2018; He FM et al., 2016; Li LY et al., 2016b; Cao X et al., 2017a, b, 2020, 2023a), resulting in the local minima of electron PSD in the radial profile in the heart of the outer radiation belt (Turner et al., 2014; Saikin et al., 2016; Shprits et al., 2017). In addition, electron scattering induced by plasmaspheric hiss is the dominant mechanism for the formation of the slot region between the inner and outer radiation belts (e.g., Li LY et al., 2021, 2022; Zhu Q et al., 2021; Cao X et al., 2023b). The magnetopause shadow effect and subsequent outward radial diffusion play a dominant role in the depletion of electrons at high L-shells (e.g., Matsumura et al., 2011; Herrera et al., 2016; Ma X et al., 2020).

An accumulated electron dataset with wider spatial and temporal coverage can be constructed from various satellites, which is essential for gaining a better understanding of the dynamic evolution of electrons in the Earth's radiation belts (Turner et al., 2012; Foster et al., 2014; Zhao H et al., 2018). Radiation belt energetic electrons pose a severe threat to the hardware systems onboard satellites (Horne et al., 2013; Lohmeyer et al., 2015; Hands et al., 2018). Hence, it is crucial to correct and properly intercalibrate the electron data measured by multiple instruments and multiple satellites before using the data to further scientific research (e.g., Kellerman et al., 2014; Park et al., 2021).

Chen Y et al. (2005, 2006) conducted intercalibrations during geomagnetically quiet times based on Liouville's theorem, which requires that PSDs be conserved at the same set of phase space coordinates (PSCs). Ni BB et al. (2009) adopted the same method to estimate cross-satellite calibration factors of the electron PSD conjunctions for one set of PSCs measured by the Akebono, Geostationary Equatorial Orbit (GEO)1989, and GEO1990 satellites based on the Combined Release and Radiation Effects Satellite (CRRES) Medium Electron Sensor A (MEA) measurements. Subsequently, Ni BB et al. (2011a) performed an energy-dependent cross-satellite calibration of the Time History of Events and Macroscale Interactions during Substorms (THEMIS) Solid State Telescope (SST) measurements over a wide range of 40–2159 keV based on Los Alamos National Laboratory (LANL)-01A satellite measurements. They suggested that the THEMIS SST instrument underestimates the electron PSDs in 40–140 keV energy channels and overestimates those for higher energies. Zhu CB et al. (2022) implemented an intercalibration between the low-Earth-orbit FengYun-3B (FY-3B) and the highly eccentric orbit Van Allen Probe-A based on electron PSD conjunctions at fixed PSCs.

Using a wealth of inner magnetospheric electron data with a period of three full solar cycles observed by multiple satellites (CRRES, Global Positioning System [GPS], GEO, and Polar), Friedel et al. (2005) presented an intercalibration by establishing a common geomagnetic coordinate and defining the "conjunction" of any two spacecraft. A series of criteria were considered, including L-shells, magnetic field strength, magnetic local time (MLT), and geomagnetic indexes. Following the method of Friedel et al. (2005), Wang CQ et al. (2013) calibrated proton and electron data

measured by polar orbit FY-3B by using a two-dimensional coordinate system (L, B) in the quiet time based on National Oceanic and Atmospheric Administration (NOAA)-17 satellite observations. Zhang Y et al. (2018) performed an L-shell-dependent cross-satellite calibration of medium-energy electrons measured by both FY-3 series satellites with Polar Orbiting Environmental Satellite (POES) measurements within 5 min × 0.1 L × 0.5 MLT. In addition, Szabó-Roberts et al. (2021) preliminarily compared the spin-averaged electron flux measurements of multiple instruments between the Arase (Exploration of energization and Radiation in Geospace [ERG]) and Van Allen Probes. They suggested that the general evolution of electron fluxes of the set of satellites show close agreement over a wide range of energy channels. The elliptical orbit Arase measurements with wide L-shell and energy coverage are considered one of the most important data sources for understanding the evolution of the Earth's radiation belts and ring current for Solar Cycle 25. Thus far, the Arase observations have been used in numerous scientific studies and have been validated by many research studies (e.g., Kurita et al., 2018; Ma Q et al., 2022; Miyoshi et al., 2022; Hartley et al., 2023). Hence, Arase observations are considered the "gold standard" of reference in this study.

FengYun-4A (FY-4A), launched on November 2016, is the newest generation of Chinese meteorological satellites (Liu Z et al., 2019). In contrast to the FY-3 series satellites, FY-4A is operating in a geosynchronous orbit, the measurements of which complement the accumulated particle dataset. Together, Arase and FY-4A provide a unique opportunity for understanding the dynamic evolution of radiation belt electrons and forecasting space weather for the upcoming solar cycle. In this study, we conduct an energy-dependent cross-satellite calibration of high-energy electron fluxes measured by the High Energy Particle Detector (HEPD) onboard FY-4A based on Arase observations spanning from April 1, 2017, to September 30, 2019.

This work is organized as follows. In Section 2, we briefly describe the instruments used, the procedures for processing data, and the definition of the conjunction. In Section 3, we present the method of cross-satellite calibration and analyze the calibration results. The major conclusions are summarized in the last section.

2. Instrument and Data Availability

Arase, launched in December 2016, is operating in an elliptical orbit with an orbital period of ~565 min and an inclination of ~31°. The perigee and apogee altitude of Arase are ~400 km and ~32,000 km, which is designed to explore the entire Earth's radiation belt zones (Miyoshi et al., 2018a, b). Level-2 definitive orbit data refer to the geomagnetic information that is calculated by using the International Radiation Belt Environment Modeling (IRBEM) library (https://prbem.github.io/IRBEM/).

Distributions of the orbits of Arase and FY-4A in the L-MLT plane with a resolution of 0.5 L × 1 h and in the L-magnetic latitude (MLAT) plane with a resolution of 0.5 L × 2.5° from April 1, 2017, to September 30, 2019 (Figure 1) reveal the potential differences in the orbits between the satellite pair. The range of L is limited to 5 to 8. The three-dimensional geomagnetic coordinate system (L, MLT, and MLAT) of FY-4A is calculated by using the Tsyganenko magnetic field model (TS04 model) applicable to geomagnetically
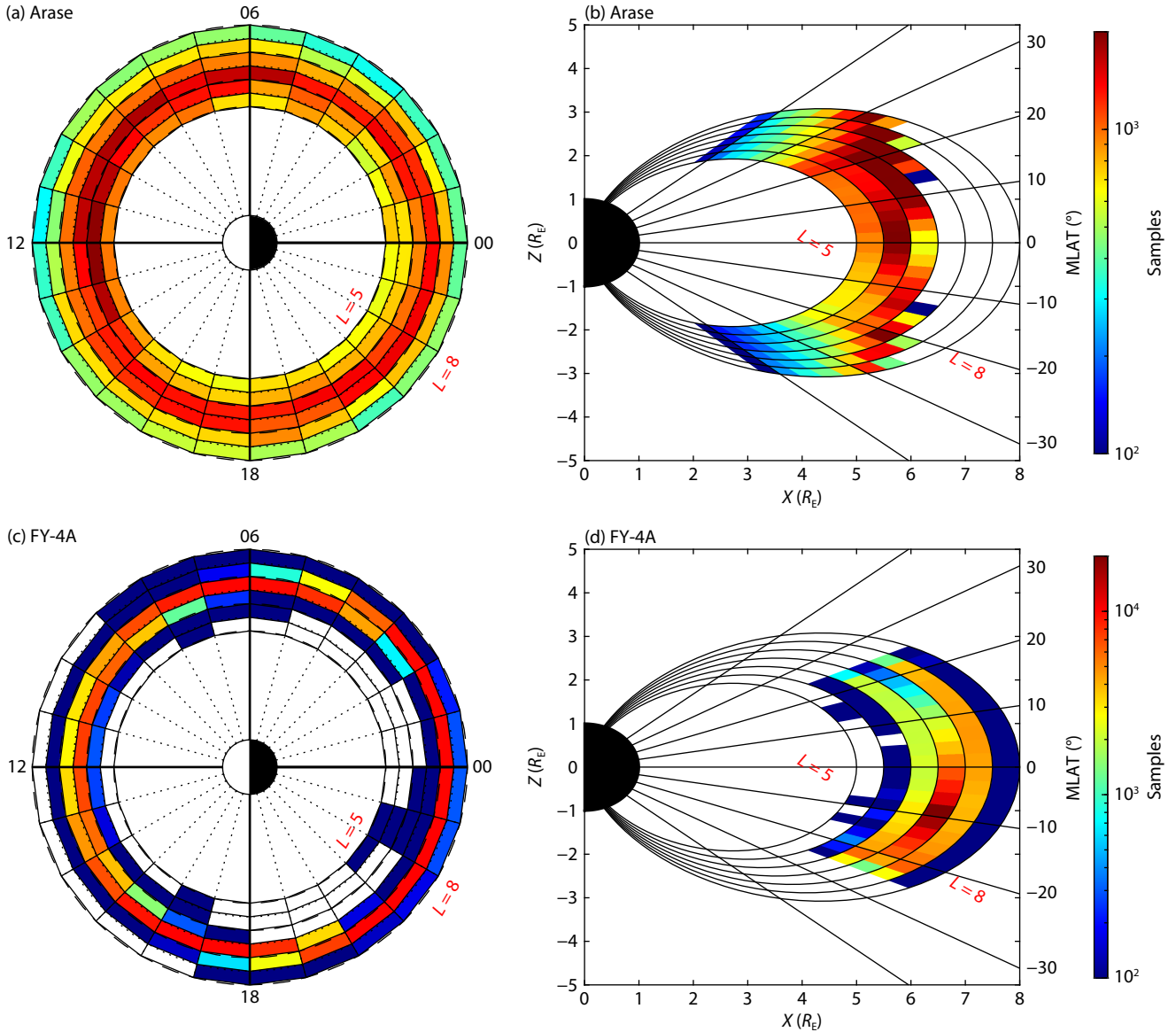
Figure 1. Distribution of the orbits of Arase and FengYun-4A (FY-4A) in the *L*-magnetic local time (MLT) plane (a and c) with a resolution of 0.5 *L* × 1 h and the *L*-magnetic latitude (MLAT) plane (b and d) with a resolution of 0.5 *L* × 2.5° from April 1, 2017, to September 30, 2019.

disturbed times (Tsyganenko and Sitnov, 2005). Compared with the elliptical orbit of Arase, which spans broader *L*-shells, the orbits for FY-4A have more points at *L* = 6.5−7.5. As shown in Figures 1a and 1c, both satellites cover all MLT regions. Figures 1b and 1d show that the two satellites operate differently near the magnetic equator. Specifically, Arase operates at *L* < 6.5, whereas FY-4A operates at higher *L* values. Moreover, FY-4A operates at an MLAT of ~ −20°−20° when *L* > 6, whereas Arase operates at larger MLAT values corresponding to lower equatorial pitch angles for the same *L*.

The High-energy Electron Experiments (HEP) instrument onboard Arase consists of two detector modules that detect the differential electron fluxes over the range of 70 keV to 1 MeV in 16 energy channels (Low unit, HEP-L) and of 700 keV to 2 MeV in 11 energy channels (High unit, HEP-H; Mitani et al., 2018; Park et al., 2021). FY-4A is equipped with three identical HEPDs (HEPD-A, HEPD-B, and HEPD-C) that face the sky direction, east direction, and west direc-

tion, respectively (Liu Z et al., 2019). Each HEPD consists of six telescopes (T1−T6) for detecting high-energy electrons and protons. Telescopes T1−T3 are used for detecting differential electron fluxes over the range of 0.2−1.5 MeV in 8 energy channels, and T4 is used for detecting integral electron fluxes in 4 energy channels. Telescopes T5 and T6 are used for detecting differential proton fluxes, including the range of 1−6.3 MeV in 3 energy channels and the range of 2−300 MeV in 8 energy channels, respectively.

To calibrate the high-energy electron fluxes derived from HEPD-B, the T1 instrument onboard FY-4A, the electron fluxes corresponding to the 90° local pitch angle measured by the HEP-L instrument onboard Arase are primarily used in this study. The original electron and orbital data measured by the satellite pair are binned over 5 min. The median of each energy channel labeled by FY-4A is obtained by $E_{ki} = 10^{[\log_{10}(E_{ki})+\log_{10}(E_{ki+1})]/2}$ (Wang CQ et al., 2013). Thus, the 6 energy channels calculated are 245, 346, 447, 548, 693, and 894 keV, respectively. Subsequently, the HEP-L instrument as a

function of energy is matched with the FY-4A energy channels by using linear interpolation in logarithms of energy (Szabó-Roberts et al., 2021). Figure 1 shows that Arase operates at higher MLAT values corresponding to lower equatorial pitch angles at the same L as FY-4A. The energetic electrons with larger equatorial pitch angles become trapped more easily by the Earth's magnetic field. To ensure that only trapped electrons are included as much as possible, we subtract the electron fluxes within 30° equatorial pitch angles.

The processed electron fluxes at the 3 selected energy channels (245, 447, and 693 keV) measured by the HEP-L instrument onboard Arase and the HEPD-B instrument onboard FY-4A from April 1 to May 31, 2017, are compared, as displayed in Figures 2a–2f. The range of L is limited to 5.5 to 7.5, which covers the orbits of FY-4A. The planetary three-hour magnetic condition

index (Kp) and symmetric horizontal component of geomagnetic disturbance (SYM-H) index with a 1-min resolution are marked by the blue line and the magenta line, respectively, in Figure 2g. Arase has a few days of missing data. Results show that the dynamic evolution of the electron fluxes measured by the satellite pair are generally consistent at the 3 different energy channels over the 2 months with moderate and intense storms occurring. Specifically, the electron fluxes at the 3 energy channels for the two satellites decrease promptly during the main phase of the moderate storm on April 4, 2017.

3. Calibration Factors from Conjunctions and Results of the Analysis

Following the aforementioned procedure, we further obtain the electron fluxes in 6 energy channels for the two satellites from
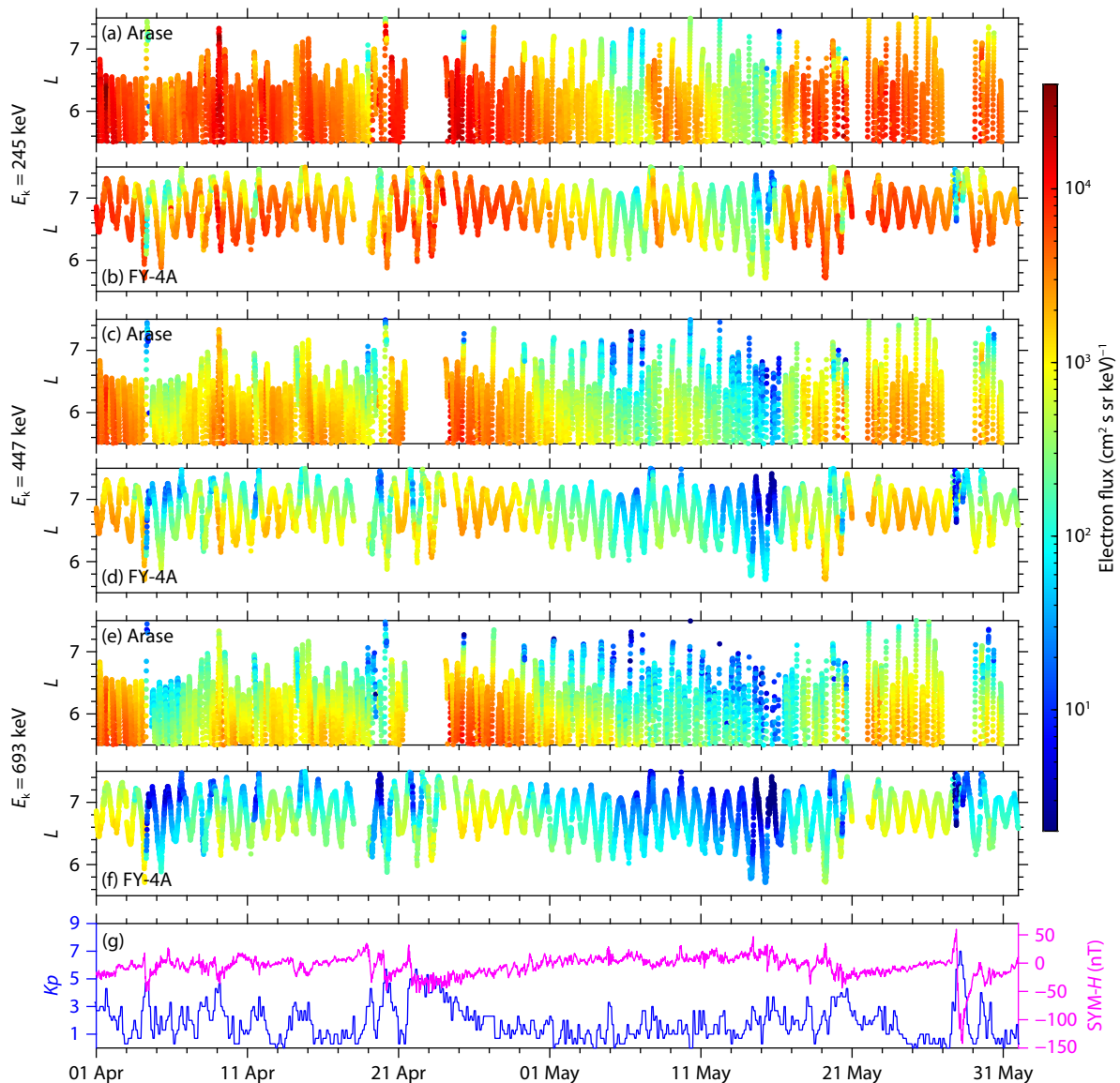

Figure 2. Comparison of electron fluxes at 3 energy channels (245, 447, and 693 keV) measured by the High-energy Electron Experiments, Low unit (HEP-L) instrument onboard Arase and the High Energy Particle Detector-B (HEPD-B) instrument onboard FY-4A (a–f), as well as the planetary three-hour magnetic condition index (Kp) and symmetric horizontal component of geomagnetic disturbance (SYM-H) index (g) from April 1 to May 31, 2017.

April 1, 2017, to September 30, 2019. By tracing the two-dimensional geomagnetic coordinate system (L, MLT) of FY-4A at each time, we can determine the electron flux conjunctions within a fixed $L \times$ MLT range. Strictly speaking, the minimum $L \times$ MLT range between the two satellites should be defined, but the number of the conjunctions is too small to obtain the statistical electron flux conjunctions. Hence, we define the electron flux conjunctions within a fixed $L \times$ MLT range with more relaxed constraints in this study. In this way, a dataset of the electron flux conjunctions with different sets of $L \times$ MLT ranges can be constructed. Furthermore, the available dataset can be selected and compared in detail.

Scatterplots of the electron flux conjunctions of Arase and FY-4A at 6 energy channels from 245 to 894 keV within three sets of $L \times$ MLT ranges are shown in Figure 3. The standard deviation (σ) of the ratio of the electron flux conjunctions in logarithms, the percentage of the ratio of the electron flux conjunctions within a factor of 2 (P), and the correlation coefficient (cc) of the electron flux conjunctions are calculated, as shown in each panel of Figure 3. The P-values are calculated as follows:

$$P = \frac{CP_1}{CP_2} \times 100\%, \tag{1}$$

where CP_1 represents the conjugate points of the ratio within a factor of 2 ($0.5 \leq$ ratio ≤ 2, ratio = $\text{Flux}_{\text{FY-4A}}/\text{Flux}_{\text{Arase}}$) and CP_2 represents the total conjugate points. $\text{Flux}_{\text{FY-4A}}$ and $\text{Flux}_{\text{Arase}}$ represent the electron flux conjunctions measured by FY-4A and Arase within a specific set of $L \times$ MLT ranges. The dashed black line

represents perfect cross-satellite agreement, and the two solid lines represent the thresholds corresponding to the ratios of the electron flux conjunctions within a factor of 2. From top to bottom, the ranges of L and MLT values increase simultaneously, and the definitions of the conjunctions are within 0.1 $L \times$ 0.5 MLT, 0.25 $L \times$ 1 MLT, and 0.5 $L \times$ 1.5 MLT, respectively. We can see that the σ values exhibit no obvious difference between 0.1 $L \times$ 0.5 MLT and 0.25 $L \times$ 1 MLT (Figures 3a–3l) and that the σ values are the largest within 0.5 $L \times$ 1.5 MLT for the fixed energy channels (Figures 3m–3r). The P-values are larger than 50% across all panels, which indicates that the electron flux conjunctions are in good agreement in general. In addition, the P-values have a significant dependence on the $L \times$ MLT ranges for the fixed energy channels. For 245 keV, the P-value becomes larger as the $L \times$ MLT range becomes smaller. All the cc values are larger than 0.5, which indicates that the variations in the electron flux conjunctions generally show close agreement. Moreover, the cc values show a significant dependence on the energy channels for the fixed $L \times$ MLT ranges. For the 0.25 $L \times$ 1 MLT range, the cc value becomes larger as the energy channel is lower.

The data points of the electron flux conjunctions at different sets of $L \times$ MLT ranges and energy channels corresponding to Figure 3 are listed in Table 1. As the $L \times$ MLT range becomes broader, all 6 energy channels have more conjugate points. Considering the three parameters calculated in Figure 3 and the number of conjugate points listed in Table 1, we conduct an energy-dependent cross-satellite calibration for the electron flux conjunctions of FY-4A within 0.25 $L \times$ 1 MLT for the statistical points. To avoid the
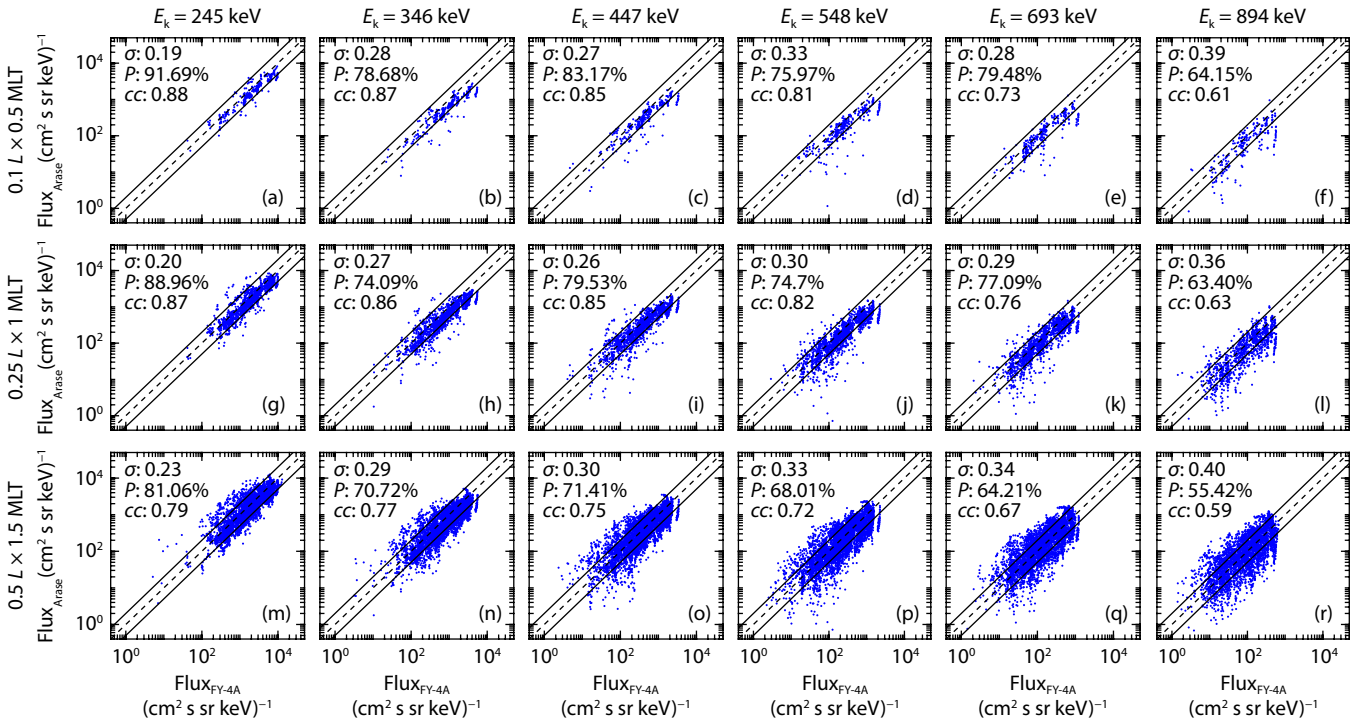

Figure 3. Scatterplots of the electron flux conjunctions of Arase and FY-4A at 6 energy channels (245–894 keV) within 0.1 $L \times$ 0.5 MLT (a–f), 0.25 $L \times$ 1 MLT (g–l), and 0.5 $L \times$ 1.5 MLT (m–r) from April 1, 2017, to September 30, 2019. In each panel, the standard deviation (σ) of the ratio of the electron flux conjunctions in logarithms, the percentage of the ratio of electron flux conjunctions within a factor of 2 (P), and the correlation coefficient (cc) of the electron flux conjunctions are labeled. The dashed black line represents perfect cross-satellite agreement, and the two solid black lines represent the thresholds corresponding to ratios of the electron flux conjunctions within a factor of 2.

Table 1. Conjugate points of Arase and FY-4A at 6 energy channels (245–894 keV) within 0.1 $L \times 0.5$ magnetic local time (MLT), 0.25 $L \times 1$ MLT, and 0.5 $L \times 1.5$ MLT from April 1, 2017, to September 30, 2019.

	Energy (keV)	245	346	447	548	693	894
Conjugate points	0.1 $L \times 0.5$ MLT	325	319	315	308	268	212
	0.25 $L \times 1$ MLT	1631	1621	1607	1569	1318	989
	0.5 $L \times 1.5$ MLT	5047	5030	4998	4898	4160	3320

effects of thermal noise, cosmic rays, and solar energetic particles on the distribution of electron fluxes, it is necessary to set reasonable thresholds for the electron flux conjunctions to ensure well-calibrated results (Friedel et al., 2005). According to the distribution of the ratios of electron flux conjunctions, the thresholds are set as ratio = 5 and ratio = 0.2 for all energy channels following the method of Zhang Y et al. (2018). The thresholds with a factor of 5 not only retain enough reliable points but also subtract less reliable points that may affect the calibration factors.

After a series of processing procedures, the high-quality electron flux conjunctions within 0.25 $L \times 1$ MLT can be used for calibrating. To quantify the differences in the electron flux conjunctions between the satellite pair at each energy channel, the normalized differences (NDs) are calculated as follows (Subbotin and Shprits, 2009):

$$ND = \frac{Flux_{FY\text{-}4A} - Flux_{Arase}}{(Flux_{FY\text{-}4A} + Flux_{Arase})/2} \times 100\% . \quad (2)$$

Comparisons of the electron flux conjunctions and NDs before and after calibration are shown in Figure 4. Histograms of the NDs before calibration are shown in Figures 4(a2)–4(f2), and the peaks of NDs are between 20% and 40% at all energy channels. The results suggest that the HEPD-B instrument onboard FY-4A systematically overestimates the electron fluxes at all 6 energy channels compared with the HEP-L instrument onboard Arase. Compared with 245–447 keV electrons, the distribution of the points of NDs corresponding to 693 and 894 keV electrons covers broader ND intervals, which also corresponds to lower cc values (Figures 3k–3l). For all energy channels, the center of the distribution of NDs corresponding to 346 keV electrons deviates more from ND = 0.

On the basis of the preceding information, we decrease the electron fluxes of FY-4A by calibration factors to match the conjugate points to different ND intervals. An optimal standard deviation (std$_o$) with electron flux conjunctions in logarithms, shown as follows, is used to determine the calibration factors:

$$std_o = \sqrt{\frac{\sum_{i=1}^{n} \log_{10}(Flux_{FY\text{-}4A} \cdot CF/Flux_{Arase})}{n}}, \quad (3)$$

where CF represents the calibration factor and n represents the number of conjugate points. By inputting a range of calibration factor values, the standard deviation values corresponding to calibration factor values can be obtained. The final calibration factor value corresponding to the minimum standard deviation value can then be determined. In this way, the cross-satellite calibration factors are determined, as listed in Table 2. The calibration factors are within a factor of 2 for all energy channels, and they differ for each energy channel. After calibration, the electron flux conjunc-

tions for the satellite pair, shown in Figures 4(a3)–4(f3), display relatively good cross-calibration agreement. The distribution of the conjugate points over the ND interval indicates that the centers of the fitted Gaussian distribution are around ND = 0 (Figures 4(a4)–4(f4)).

The collected electron flux conjunctions at all six energy channels are displayed in Figures 5a and 5b. There is a better agreement between the electron fluxes measured by FY-4A and Arase after calibration compared to those before calibration. Additionally, following Ni BB et al. (2011a), the normalized root mean square errors (NRMSE) are calculated by using the following equation

$$NRMSE = \frac{\sqrt{\sum_{i=1}^{n}[(Flux_{FY\text{-}4A})_i - (Flux_{Arase})_i]^2/n}}{\sqrt{std\,(Flux_{FY\text{-}4A})} \cdot \sqrt{std\,(Flux_{Arase})}}, \quad (4)$$

where std represents the standard deviation. Comparisons of the NRMSE values at all 6 energy channels before (blue lines) and after (magenta lines) calibration are shown in Figure 5c. Before calibration, the highest NRMSE value occurs at 346 keV owing to the worse agreement in P-values, as shown in Figure 3h, and asymmetric distributions of the points of NDs that deviated from ND = 0, as shown in Figure 4(b2). It is obvious that the NRMSE values become much smaller at all energy channels after calibration and have a significant dependence on the energy channels. Larger errors occur at higher energy channels of the HEPD-B instrument, as shown by the broader coverages of the electron flux conjunctions in the scatterplots (Figures 4(e3)–4(f3)) and in the distributions of the ND points (Figures 4(e4)–4(f4)).

4. Conclusions

In this study, we conduct an energy-dependent cross-satellite calibration of high-energy electron fluxes measured by the HEPD instrument onboard the Earth's synchronous orbit FY-4A spanning from April 1, 2017, to September 30, 2019. Measurements by the HEP instrument onboard Arase in elliptical orbit are primarily used as the "gold standard" owing to the high quality of the electron flux data. By tracing the two-dimensional magnetic positions (L, MLT) of FY-4A at each time, we construct a dataset of electron flux conjunctions over the range of 245–894 keV in 6 energy channels between the satellite pair within different sets of $L \times$ MLT ranges.

The major conclusions are summarized as follows:

(1) The variations in electron flux conjunctions between FY-4A and Arase exhibit good agreement. The percentages of ratios of electron flux conjunctions within a factor of 2 are larger than 50%, showing a significant $L \times$ MLT dependence.

(2) Systematic errors in the electron fluxes in the energy range of 245–894 keV measured by FY-4A within 0.25 $L \times 1$ MLT are esti-
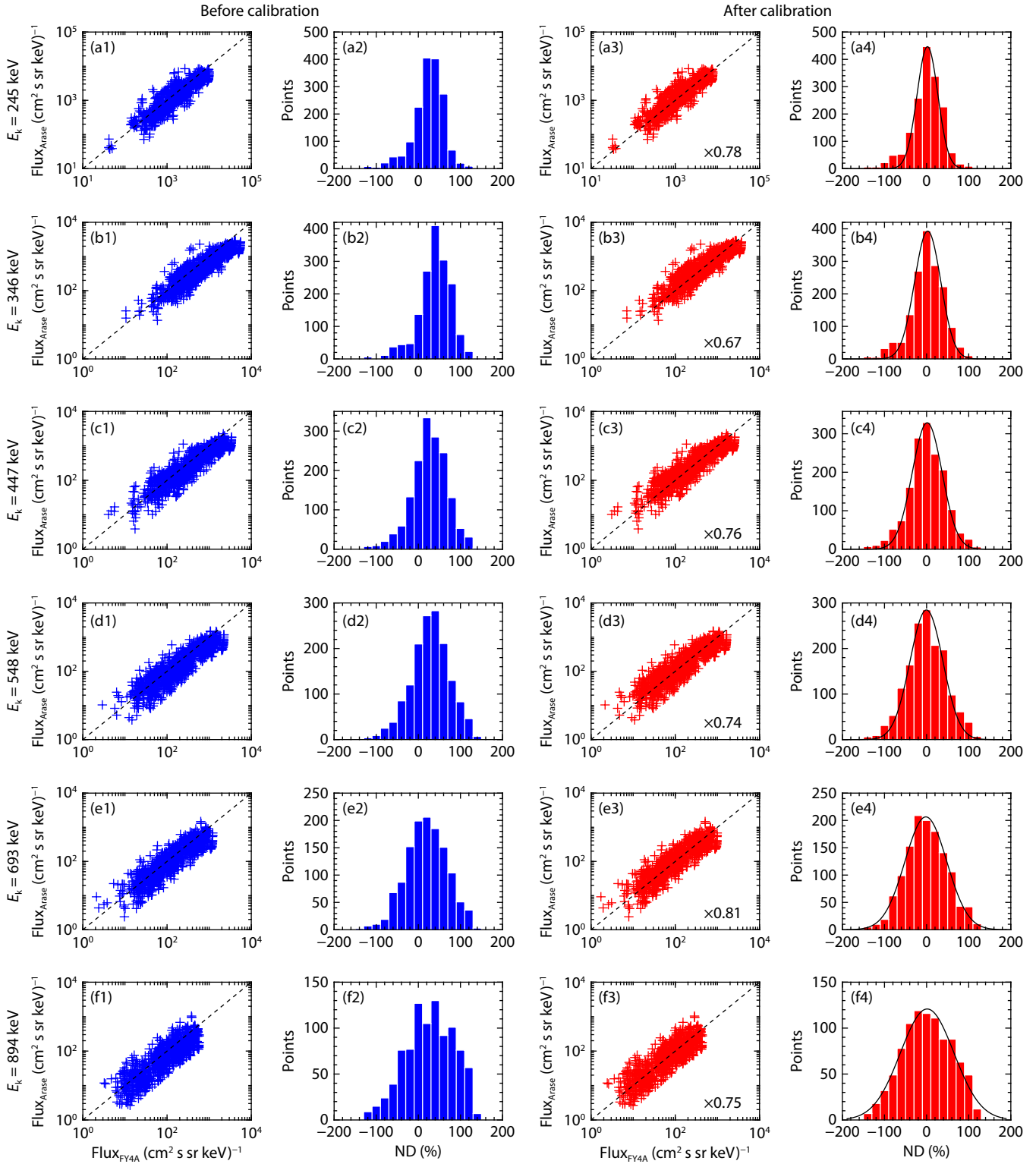
Figure 4. Comparisons between electron fluxes and their normalized differences (ND) before (a1–f2) and after (a3–f4) calibration. The solid black lines represent the fitted Gaussian distributions.

Table 2. Calibration factors of the High Energy Particle Detector-B instrument onboard FY-4A as a function of energy based on the electron flux conjunctions with the High-energy Electron Experiments-Low unit instrument onboard Arase.

Energy (keV)	245	346	447	548	693	894
Calibration factor	0.78	0.67	0.76	0.74	0.81	0.75

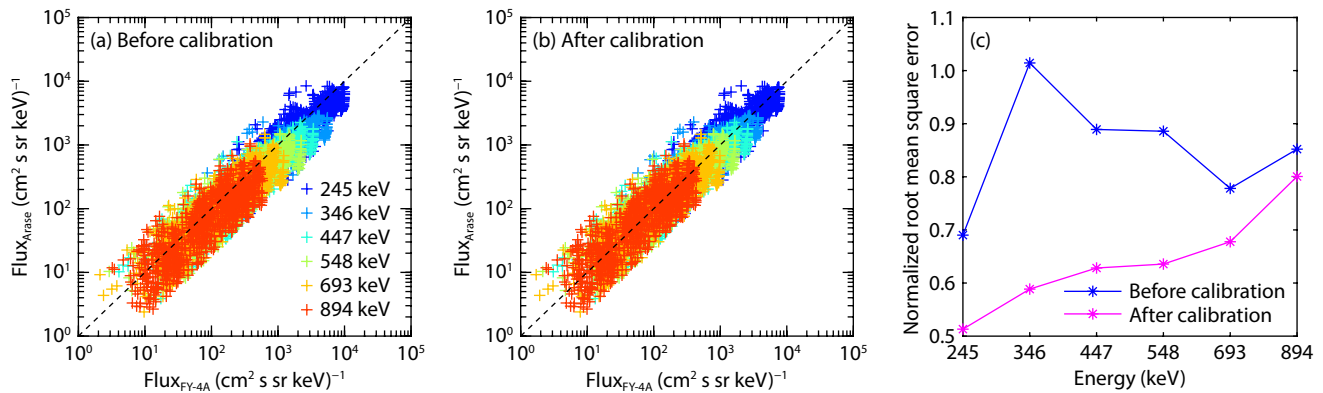**Wang XY, Cao X and Ma X et al.: Cross-satellite calibration of FY-4A**

Figure 5. Comparisons of the electron flux conjunctions (a–b) before and after calibration and their normalized root mean square errors (c) as a function of electron energy.

mated. Compared with Arase, FY-4A systematically overestimates electron fluxes at all 6 energy channels, and the corresponding calibration factors are 0.67–0.81.

(3) The conjugate electron fluxes for the satellite pair show better agreement after calibration, as well as much smaller NRMSE for all 6 energy channels. The NRMSE values after calibration tend to increase monotonically as electron energy increases.

Acknowledgments

References

Allison, H. J., and Shprits, Y. Y. (2020). Local heating of radiation belt electrons to ultra-relativistic energies. *Nat. Commun.*, *11*(1), 4533. https://doi.org/ 10.1038/s41467-020-18053-z

Aseev, N. A., Shprits, Y. Y., Drozdov, A. Y., Kellerman, A. C., Usanova, M. E., Wang, D., and Zhelavskaya, I. S. (2017). Signatures of ultrarelativistic electron loss in the heart of the outer radiation belt measured by Van Allen Probes. *J. Geophys. Res.: Space Phys.*, *122*(10), 10102–10111. https://doi.org/10.1002/ 2017JA024485

Baker, D. N. (2021). Wave–particle interaction effects in the Van Allen belts.

Earth Planets Space, *73*(1), 189. https://doi.org/10.1186/s40623-021-01508-y

Birn, J., Thomsen, M. F., Borovsky, J. E., Reeves, G. D., McComas, D. J., and Belian, R. D. (1997). Characteristic plasma properties during dispersionless substorm injections at geosynchronous orbit. *J. Geophys. Res.: Space Phys.*, *102*(A2), 2309–2324. https://doi.org/10.1029/96JA02870

Boakes, P. D., Milan, S. E., Abel, G. A., Freeman, M. P., Chisham, G., and Hubert, B. (2011). A superposed epoch investigation of the relation between magnetospheric solar wind driving and substorm dynamics with geosynchronous particle injection signatures. *J. Geophys. Res.: Space Phys.*, *116*(A1), A01214. https://doi.org/10.1029/2010JA016007

Boyd, A. J., Turner, D. L., Reeves, G. D., Spence, H. E., Baker, D. N., and Blake, J. B. (2018). What causes radiation belt enhancements: A survey of the Van Allen Probes era. *Geophys. Res. Lett.*, *45*(11), 5253–5259. https://doi.org/10.1029/ 2018GL077699

Cao, J. B., Wei, X. H., Duan, A. Y., Fu, H. S., Zhang, T. L., Reme, H., and Dandouras, I. (2013). Slow magnetosonic waves detected in reconnection diffusion region in the Earth's magnetotail. *J. Geophys. Res.: Space Phys.*, *118*(4), 1659–1666. https://doi.org/10.1002/jgra.50246

Cao, X., Ni, B. B., Summers, D., Bortnik, J., Tao, X., Shprits, Y. Y., Lou, Y. Q., Gu, X. D., Fu, S., ... Wang, Q. (2017a). Bounce resonance scattering of radiation belt electrons by H+ band EMIC waves. *J. Geophys. Res.: Space Phys.*, *122*(2), 1702–1713. https://doi.org/10.1002/2016JA023607

Cao, X., Ni, B. B., Summers, D., Zou, Z. Y., Fu, S., and Zhang, W. X. (2017b). Bounce resonance scattering of radiation belt electrons by low-frequency hiss: Comparison with cyclotron and Landau resonances. *Geophys. Res. Lett.*, *44*(19), 9547–9554. https://doi.org/10.1002/2017GL075104

Cao, X., Ni, B. B., Summers, D., Shprits, Y. Y., and Lou, Y. Q. (2020). Effects of polarization reversal on the pitch angle scattering of radiation belt electrons and ring current protons by EMIC waves. *Geophys. Res. Lett.*, *47*(17), e2020GL089718. https://doi.org/10.1029/2020GL089718

Cao, X., Lu, P., Ni, B. B., Summers, D., Shprits, Y. Y., Long, M. Y., and Wang, X. Y. (2023a). Resonant scattering of radiation belt electrons at Saturn by ion cyclotron waves. *Geophys. Res. Lett.*, *50*(3), e2022GL102394. https://doi.org/ 10.1029/2022GL102394

Cao, X., Lu, P., Zhu, Q., Ma, X., and Ni, B. B. (2023b). Bounce resonance scattering of slot region electrons by plasmaspheric hiss. *Chin. J. Geophys.* (in Chinese), *66*(5), 1796–1806. https://doi.org/10.6038/cjg2022Q0669

Chen, Y., Friedel, R. H. W., Reeves, G. D., Onsager, T. G., and Thomson, M. F. (2005). Multisatellite determination of the relativistic electron phase space density at geosynchronous orbit: Methodology and results during geomagnetically quiet times. *J. Geophys. Res.: Space Phys.*, *110*(A10), A10210. https://doi.org/10.1029/2004JA010895

Chen, Y., Friedel, R. H. W., and Reeves, G. D. (2006). Phase space density distributions of energetic electrons in the outer radiation belt during two Geospace Environment Modeling Inner Magnetosphere/Storms selected storms. *J. Geophys. Res.: Space Phys.*, *111*(A11), A11S04. https://doi.org/ 10.1029/2006JA011703

Chen, Y., Reeves, G. D., and Friedel, R. H. W. (2007). The energization of relativistic electrons in the outer Van Allen radiation belt. *Nat. Phys.*, *3*(9), 614–617. https://doi.org/10.1038/nphys655

Foster, J. C., Erickson, P. J., Baker, D. N., Claudepierre, S. G., Kletzing, C. A., Kurth, W., Reeves, G. D., Thaller, S. A., Spence, H. E., … Wygant, J. R. (2014). Prompt energization of relativistic and highly relativistic electrons during a substorm interval: Van Allen Probes observations. *Geophys. Res. Lett.*, *41*(1), 20–25. https://doi.org/10.1002/2013GL058438

Friedel, R. H. W., Bourdarie, S., and Cayton, T. E. (2005). Intercalibration of magnetospheric energetic electron data. *Space Weather*, *3*(9), S09B04. https://doi.org/10.1029/2005sw000153

Gao, Z. L., Su, Z. P., Xiao, F. L., Zheng, H. N., Wang, Y. M., Wang, S., Spence, H. E., Reeves, G. D., Baker, D. N., … Funsten, H. O. (2018). Exohiss wave enhancement following substorm electron injection in the dayside magnetosphere. *Earth Planet. Phys.*, *2*(5), 359–370. https://doi.org/10.26464/epp2018033

Gu, X. D., Xia, S. J., Fu, S., Xiang, Z., Ni, B. B., Guo, J. G., and Cao, X. (2020). Dynamic responses of radiation belt electron fluxes to magnetic storms and their correlations with magnetospheric plasma wave activities. *Astrophys. J.*, *891*(2), 127. https://doi.org/10.3847/1538-4357/ab71fc

Hands, A. D. P., Ryden, K. A., Meredith, N. P., Glauert, S. A., and Horne, R. B. (2018). Radiation effects on satellites during extreme space weather events. *Space Weather*, *16*(9), 1216–1226. https://doi.org/10.1029/2018SW001913

Hartley, D. P., Cunningham, G. S., Ripoll, J. F., Malaspina, D. M., Kasahara, Y., Miyoshi, Y., Matsuda, S., Nakamura, S., Tsuchiya, F., … Matsuoka, A. (2023). Using Van Allen Probes and Arase observations to develop an empirical plasma density model in the inner zone. *J. Geophys. Res.: Space Phys.*, *128*(3), e2022JA031012. https://doi.org/10.1029/2022JA031012

He, F. M., Cao, X., Ni, B. B., Xiang, Z., Zhou, C., Gu, X. D., Zhao, Z. Y., Shi, R., and Wang, Q. (2016). Combined scattering loss of radiation belt relativistic electrons by simultaneous three-band EMIC waves: A case study. *J. Geophys. Res.: Space Phys.*, *121*(5), 4446–4451. https://doi.org/10.1002/2016JA022483

He, J. B., Jin, Y. Y., Xiao, F. L., He, Z. G., Yang, C., Xie, Y. Q., He, Q., Wang, C. Z., Shang, X. J., … Zhang, S. (2021). The influence of various frequency chorus waves on electron dynamics in radiation belts. *Sci. China Technol. Sci.*, *64*(4), 890–897. https://doi.org/10.1007/s11431-020-1750-6

He, Q., Liu, S., Xiao, F. L., Gao, Z. L., Li, T., Shang, X. J., Zhou, Q. H., Yang, C., and He, Y. H. (2022). Observations and parametric study on the role of plasma density on extremely low-frequency chorus wave generation. *Sci. China Technol. Sci.*, *65*(11), 2649–2657. https://doi.org/10.1007/s11431-021-2030-7

Herrera, D., Maget, V. F., and Sicard-Piet, A. (2016). Characterizing magnetopause shadowing effects in the outer electron radiation belt during geomagnetic storms. *J. Geophys. Res.: Space Phys.*, *121*(10), 9517–9530. https://doi.org/10.1002/2016JA022825

Horne, R. B., Thorne, R. M., Shprits, Y. Y., Meredith, N. P., Glauert, S. A., Smith, A. J., Kanekal, S. G., Baker, D. N., Engebretson, M. J., … Decreau, P. M. E. (2005). Wave acceleration of electrons in the Van Allen radiation belts. *Nature*, *437*(7056), 227–230. https://doi.org/10.1038/nature03939

Horne, R. B., Thorne, R. M., Glauert, S. A., Meredith, N. P., Pokhotelov, D., and Santolík, O. (2007). Electron acceleration in the Van Allen radiation belts by fast magnetosonic waves. *Geophys. Res. Lett.*, *34*(17), L17107. https://doi.org/10.1029/2007GL030267

Horne, R. B., Glauert, S. A., Meredith, N. P., Boscher, D., Maget, V., Heynderickx, D., and Pitchford, D. (2013). Space weather impacts on satellites and forecasting the Earth's electron radiation belts with SPACECAST. *Space Weather*, *11*(4), 169–186. https://doi.org/10.1002/swe.20023

Kellerman, A. C., Shprits, Y. Y., Kondrashov, D., Subbotin, D., Makarevich, R. A., Donovan, E., and Nagai, T. (2014). Three-dimensional data assimilation and reanalysis of radiation belt electrons: Observations of a four-zone structure using five spacecraft and the VERB code. *J. Geophys. Res.: Space Phys.*, *119*(11), 8764–8783. https://doi.org/10.1002/2014JA020171

Kurita, S., Miyoshi, Y., Shiokawa, K., Higashio, N., Mitani, T., Takashima, T., Matsuoka, A., Shinohara, I., Kletzing, C. A., … Otsuka, Y. (2018). Rapid loss of relativistic electrons by EMIC waves in the outer radiation belt observed by Arase, Van Allen Probes, and the PWING ground stations. *Geophys. Res. Lett.*, *45*(23), 12720–12729. https://doi.org/10.1029/2018GL080262

Li, L. Y., Cao, J. B., Zhou, G. C., and Li, X. (2009). Statistical roles of storms and substorms in changing the entire outer zone relativistic electron population. *J. Geophys. Res.: Space Phys.*, *114*(A12), A12214. https://doi.org/10.1029/2009JA014333

Li, L. Y., Cao, J. B., Yang, J. Y., and Dong, Y. X. (2013). Joint responses of geosynchronous magnetic field and relativistic electrons to external changes in solar wind dynamic pressure and interplanetary magnetic field. *J. Geophys. Res.: Space Phys.*, *118*(4), 1472–1482. https://doi.org/10.1002/jgra.50201

Li, L. Y., Yu, J., Cao, J. B., Wang, Z. Q., Yu, Y. Q., Reeves, G. D., and Li, X. (2016a). Effects of ULF waves on local and global energetic particles: Particle energy and species dependences. *J. Geophys. Res.: Space Phys.*, *121*(11), 11007–11020. https://doi.org/10.1002/2016JA023149

Li, L. Y., Yu, J., Cao, J. B., and Yuan, Z. G. (2016b). Compression‐amplified EMIC waves and their effects on relativistic electrons. *Phys. Plasmas*, *23*(6), 062116. https://doi.org/10.1063/1.4953899

Li, L. Y., Yu, J., Cao, J. B., Yang, J. Y., Li, X., Baker, D. N., Reeves, G. D., and Spence, H. (2017). Roles of whistler mode waves and magnetosonic waves in changing the outer radiation belt and the slot region. *J. Geophys. Res.: Space Phys.*, *122*(5), 5431–5448. https://doi.org/10.1002/2016JA023634

Li, L. Y., and Wang, Z. Q. (2018). The effects of solar wind dynamic pressure changes on the substorm auroras and energetic electron injections on 24 August 2005. *J. Geophys. Res.: Space Phys.*, *123*(1), 385–399. https://doi.org/10.1002/2017JA024628

Li, L. Y., Yang, S. S., Cao, J. B., Yu, J., Luo, X. Y., and Blake, J. B. (2019). Effects of solar wind plasma flow and interplanetary magnetic field on the spatial structure of Earth's radiation belts. *J. Geophys. Res.: Space Phys.*, *124*(12), 10332–10344. https://doi.org/10.1029/2019JA027284

Li, L. Y., Wang, Z. Y., Yu, J., and Cao, J. B. (2021). Complementary and catalytic roles of man-made VLF waves and natural plasma waves in the loss of radiation belt electrons. *J. Geophys. Res.: Space Phys.*, *126*(10), e2020JA028879. https://doi.org/10.1029/2020JA028879

Li, L. Y., Yu, J., Cao, J. B., Chen, L. J., Reeves, G. D., and Blake, J. B. (2022). Competitive influences of different plasma waves on the pitch angle distribution of energetic electrons inside and outside plasmasphere. *Geophys. Res. Lett.*, *49*(1), e2021GL096062. https://doi.org/10.1029/2021GL096062

Li, W., Ma, Q., Thorne, R. M., Bortnik, J., Zhang, X. J. , Li, J., Baker, D. N., Reeves, G. D., Spence, H. E., … Goldstein, J. (2016). Radiation belt electron acceleration during the 17 March 2015 geomagnetic storm: Observations and simulations. *J. Geophys. Res.: Space Phys.*, *121*(6), 5520–5536. https://doi.org/10.1002/2016JA022400

Liu, Z., Yang, X. C., Zhang, X. X., Zhang, K. Y., Yu, Q. L., Zhang, X., Xue, B. S., Guo, J. G., Zong, W. G., … Ji, W. T. (2019). On-orbit cross-calibration and assimilation for relativistic electron observations from FengYun 4A and GOES-13. *Acta Phys. Sin.*, *68*(15), 159401. https://doi.org/10.7498/aps.68.20190433

Lohmeyer, W., Carlton, A., Wong, F., Bodeau, M., Kennedy, A., and Cahoy, K. (2015). Response of geostationary communications satellite solid-state power amplifiers to high-energy electron fluence. *Space Weather*, *13*(5), 298–315. https://doi.org/10.1002/2014SW001147

Ma, Q., Xu, W., Sanchez, E. R., Marshall, R. A., Bortnik, J., Reyes, P. M., Varney, R. H., Kaeppler, S. R., Miyoshi, Y., … Tam, S. W. Y. (2022). Analysis of electron precipitation and ionospheric density enhancements due to hiss using incoherent scatter radar and Arase observations. *J. Geophys. Res.: Space Phys.*, *127*(8), e2022JA030545. https://doi.org/10.1029/2022JA030545

Ma, Q. L., Li, W., Thorne, R. M., Bortnik, J., Kletzing, C. A., Kurth, W. S., and Hospodarsky, G. B. (2016). Electron scattering by magnetosonic waves in the inner magnetosphere. *J. Geophys. Res.: Space Phys.*, *121*(1), 274–285. https://doi.org/10.1002/2015JA021992

Ma, X., Xiang, Z., Ni, B. B., Fu, S., Cao, X., Hua, M., Guo, D. Y., Guo, Y. J., Gu, X. D., … Zhu, Q. (2020). On the loss mechanisms of radiation belt electron dropouts during the 12 September 2014 geomagnetic storm. *Earth Planet. Phys.*, *4*(6), 598–610. https://doi.org/10.26464/epp2020060

Matsumura, C., Miyoshi, Y., Seki, K., Saito, S., Angelopoulos, V., and Koller, J. (2011). Outer radiation belt boundary location relative to the magnetopause: Implications for magnetopause shadowing. *J. Geophys. Res.:*

Space Phys., 116(A6), A06212. https://doi.org/10.1029/2011JA016575

Mitani, T., Takashima, T., Kasahara, S., Miyake, W., and Hirahara, M. (2018). High-energy electron experiments (HEP) aboard the ERG (Arase) satellite. *Earth Planets Space*, 70, 77. https://doi.org/10.1186/s40623-018-0853-1

Miyoshi, Y. S., Jordanova, V. K., Morioka, A., and Evans, D. D. (2004). Solar cycle variations of the electron radiation belts: Observations and radial diffusion simulation. *Space Weather*, 2(10), S10S02. https://doi.org/10.1029/2004SW000070

Miyoshi, Y., Shinohara, I., Takashima, T., Asamura, K., Higashio, N., Mitani, T., Kasahara, S., Yokota, S., Kazama, Y., ... Seki, K. (2018a). Geospace exploration project ERG. *Earth Planets Space*, 70(1), 101. https://doi.org/10.1186/s40623-018-0862-0

Miyoshi, Y., Hori, T., Shoji, M., Teramoto, M., Chang, T. F., Segawa, T., Umemura, N., Matsuda, S., Kurita, S., ... Shinohara, I. (2018b). The ERG science center. *Earth Planets Space*, 70(1), 96. https://doi.org/10.1186/s40623-018-0867-8

Miyoshi, Y., Shinohara, I., Ukhorskiy, S., Claudepierre, S. G., Mitani, T., Takashima, T., Hori, T., Santolik, O., Kolmasova, I., ... Lanzerotti, L. (2022). Collaborative research activities of the Arase and Van Allen Probes. *Space Sci. Rev.*, 218(5), 38. https://doi.org/10.1007/s11214-022-00885-4

Nagai, T., Shinohara, I., Singer, H. J., Rodriguez, J., and Onsager, T. G. (2019). Proton and electron injection path at geosynchronous altitude. *J. Geophys. Res.: Space Phys.*, 124(6), 4083–4103. https://doi.org/10.1029/2018JA026281

Ni, B. B., Shprits, Y., Thorne, R., Friedel, R., and Nagai, T. (2009). Reanalysis of relativistic radiation belt electron phase space density using multisatellite observations: Sensitivity to empirical magnetic field models. *J. Geophys. Res.: Space Phys.*, 114(A12), A12208. https://doi.org/10.1029/2009JA014438

Ni, B. B., Shprits, Y., Hartinger, M., Angelopoulos, V., Gu, X. D., and Larson, D. (2011a). Analysis of radiation belt energetic electron phase space density using THEMIS SST measurements: Cross-satellite calibration and a case study. *J. Geophys. Res.: Space Phys.*, 116(A3), A03208. https://doi.org/10.1029/2010JA016104

Ni, B. B., Thorne, R. M., Meredith, N. P., Shprits, Y. Y., and Horne, R. B. (2011b). Diffuse auroral scattering by whistler mode chorus waves: Dependence on wave normal angle distribution. *J. Geophys. Res.: Space Phys.*, 116(A10), A10207. https://doi.org/10.1029/2011JA016517

Ni, B. B., Cao, X., Zou, Z. Y., Zhou, C., Gu, X. D., Bortnik, J., Zhang, J. C., Fu, S., Zhao, Z. Y., ... Xie, L. (2015). Resonant scattering of outer zone relativistic electrons by multiband EMIC waves and resultant electron loss time scales. *J. Geophys. Res.: Space Phys.*, 120(9), 7357–7373. https://doi.org/10.1002/2015JA021466

Ni, B. B., Cao, X., Shprits, Y. Y., Summers, D., Gu, X. D., Fu, S., and Lou, Y. Q. (2018). Hot plasma effects on the cyclotron-resonant pitch-angle scattering rates of radiation belt electrons due to EMIC waves. *Geophys. Res. Lett.*, 45(1), 21–30. https://doi.org/10.1002/2017GL076028

Ni, B. B., Summers, D., Xiang, Z., Dou, X. K., Tsurutani, B., Meredith, N. P., Dong, J. H., Chen, L. J., Reeves, G. D., ... Xu, W. (2023). Unique banded structures of plasmaspheric hiss waves in the Earth's magnetosphere. *J. Geophys. Res.: Space Phys.*, 128(3), e2023JA031325. https://doi.org/10.1029/2023JA031325

Ni, B., Yan, L., Fu, S., Gu, X., Cao, X., Xiang, Z., and Zhang, Y. (2020). Distinct formation and evolution characteristics of outer radiation belt electron butterfly pitch angle distributions observed by Van Allen Probes. *Geophys. Res. Lett.*, 47(4), e2019GL086487. https://doi.org/10.1029/2019GL086487

Park, I., Miyoshi, Y., Mitani, T., Hori, T., Takashima, T., Kurita, S., Shinohara, I., Kasahara, S., Yokota, S., ... Looper, M. D. (2021). Characterization and calibration of high-energy electron instruments onboard the Arase satellite. *J. Geophys. Res.: Space Phys.*, 126(7), e2021JA029110. https://doi.org/10.1029/2021JA029110

Saikin, A. A., Zhang, J. C., Smith, C. W., Spence, H. E., Torbert, R. B., and Kletzing, C. A. (2016). The dependence on geomagnetic conditions and solar wind dynamic pressure of the spatial distributions of EMIC waves observed by the Van Allen Probes. *J. Geophys. Res.: Space Phys.*, 121(5), 4362–4377. https://doi.org/10.1002/2016JA022523

Shprits, Y. Y., Elkington, S. R., Meredith, N. P., and Subbotin, D. A. (2008). Review of modeling of losses and sources of relativistic electrons in the outer radiation belt I: Radial transport. *J. Atmos. Sol.-Terr. Phys.*, 70(14), 1679–1693. https://doi.org/10.1016/j.jastp.2008.06.008

Shprits, Y. Y., Kellerman, A., Aseev, N., Drozdov, A. Y., and Michaelis, I. (2017). Multi-MeV electron loss in the heart of the radiation belts. *Geophys. Res. Lett.*, 44(3), 1204–1209. https://doi.org/10.1002/2016GL072258

Su, Z. P., Zhu, H., Xiao, F. L., Zong, Q. G., Zhou, X. Z., Zheng, H. N., Wang, Y. M., Wang, S., Hao, Y. X., ... Wygant, J. R. (2015). Ultra-low-frequency wave-driven diffusion of radiation belt relativistic electrons. *Nat. Commun.*, 6, 10096. https://doi.org/10.1038/ncomms10096

Subbotin, D. A., and Shprits, Y. Y. (2009). Three-dimensional modeling of the radiation belts using the versatile electron radiation belt (VERB) code. *Space Weather*, 7(10), S10001. https://doi.org/10.1029/2008SW000452

Szabó-Roberts, M., Shprits, Y. Y., Allison, H. J., Vasile, R., Smirnov, A. G., Aseev, N. A., Drozdov, A. Y., Miyoshi, Y., Claudepierre, S. G., ... Shinohara, I. (2021). Preliminary statistical comparisons of spin-averaged electron data from Arase and Van Allen Probes instruments. *J. Geophys. Res.: Space Phys.*, 126(7), e2020JA028929. https://doi.org/10.1029/2020JA028929

Tang, C. L., Wang, X., Ni, B. B., Su, Z. P., and Zhang, J. C. (2022). The 600 keV electron injections in the Earth's outer radiation belt: A statistical study. *Earth Planet. Phys.*, 6(2), 149–160. https://doi.org/10.26464/epp2022012

Tang, R. X., Yuan, A., Li, H. M., Ouyang, Z. H., and Deng, X. H. (2023). Influence of solar wind dynamic pressure on distribution of whistler mode waves based on Van Allen Probe observations. *J. Geophys. Res.: Space Phys.*, 128(4), e2022JA031181. https://doi.org/10.1029/2022JA031181

Thorne, R. M., Li, W., Ni, B., Ma, Q., Bortnik, J., Chen, L., Baker, D. N., Spence, H. E., Reeves, G. D., ... Kanekal, S. G. (2013). Rapid local acceleration of relativistic radiation-belt electrons by magnetospheric chorus. *Nature*, 504(7480), 411–414. https://doi.org/10.1038/nature12889

Tsyganenko, N. A., and Sitnov, M. I. (2005). Modeling the dynamics of the inner magnetosphere during strong geomagnetic storms. *J. Geophys. Res.: Space Phys.*, 110(A3), A03208. https://doi.org/10.1029/2004JA010798

Turner, D. L., Shprits, Y., Hartinger, M., and Angelopoulos, V. (2012). Explaining sudden losses of outer radiation belt electrons during geomagnetic storms. *Nat. Phys.*, 8(3), 208–212. https://doi.org/10.1038/nphys2185

Turner, D. L., Angelopoulos, V., Li, W., Bortnik, J., Ni, B., Ma, Q., Thorne, R. M., Morley, S. K., Henderson, M. G., ... Rodriguez, J. V. (2014). Competing source and loss mechanisms due to wave–particle interactions in Earth's outer radiation belt during the 30 September to 3 October 2012 geomagnetic storm. *J. Geophys. Res.: Space Phys.*, 119(3), 1960–1979. https://doi.org/10.1002/2014JA019770

Wang, C. Q., Zhang, X. G., Li, J. W., Huang, C., Zhang, X. X., Jing, T., Shen, G. H., Zhang, S. Y., Cao, G. W., ... Han, Y. (2013). Cross-calibration of high energetic particles data—A case study between FY-3B and NOAA-17. *Sci. China Technol. Sci.*, 56(11), 2668–2674. https://doi.org/10.1007/s11431-013-5375-2

Wang, X. Y., Cao, X., Gu, X. D., Ni, B. B., Ma, X., Luo, T., and Guo, D. Y. (2023). Prompt enhancements of radiation belt electrons over a wide energy range based on phase space density variations: A detailed case study. *Astrophys. J.*, 942(1), 30. https://doi.org/10.3847/1538-4357/aca4c7

Xiang, Z., Tu, W. C., Ni, B. B., Henderson, M. G., and Cao, X. (2018). A statistical survey of radiation belt dropouts observed by Van Allen Probes. *Geophys. Res. Lett.*, 45(16), 8035–8043. https://doi.org/10.1029/2018GL078907

Xiao, F. L., Liu, S., Tao, X., Su, Z. P., Zhou, Q. H., Yang, C., He, Z. G., He, Y. H., Gao, Z. L., ... Blake, J. B. (2017). Generation of extremely low frequency chorus in Van Allen radiation belts. *J. Geophys. Res.: Space Phys.*, 122(3), 3201–3211. https://doi.org/10.1002/2016JA023561

Xiong, Y., Xie, L., Fu, S. Y., Ni, B. B., and Pu, Z. Y. (2021). Non-storm erosion of MeV electron outer radiation belt down to $L^* < 4.0$ associated with successive enhancements of solar wind density. *Earth Planet. Phys.*, 5(6), 581–591. https://doi.org/10.26464/epp2021051

Yang, C., Wang, Z. Q., Xiao, F. L., He, Z. G., Xie, Y. Q., Zhang, S., He, Y. H., Liu, S., and Zhou, Q. H. (2022). Correlated observations linking loss of energetic protons to EMIC waves. *Sci. China Technol. Sci.*, 65(1), 131–138. https://doi.org/10.1007/s11431-021-1882-x

Yue, C., Ma, Q. L., Jun, C. W., Bortnik, J., Zong, Q. G., Zhou, X. Z., Jang, E., Reeves, G. D., Spence, H. E., ... Wygant, J. R. (2020). The modulation of plasma and waves by background electron density irregularities in the inner magnetosphere. *Geophys. Res. Lett.*, 47(15), e2020GL088855. https://doi.org

/10.1029/2020GL088855

Zhang, Y., Ni, B. B., Xiang, Z., Zhang, X. G., Zhang, X. X., Gu, X. D., Fu, S., Cao, X., and Zou, Z. Y. (2018). Inter-satellite calibration of FengYun 3 medium energy electron fluxes with POES electron measurements. *Adv. Space Res., 61*(9), 2290–2300. https://doi.org/10.1016/j.asr.2018.02.017

Zhao, H., Baker, D. N., Li, X., Jaynes, A. N., and Kanekal, S. G. (2018). The acceleration of ultrarelativistic electrons during a small to moderate storm of 21 April 2017.. *Geophys. Res. Lett., 45*(12), 5818–5825. https://doi.org/10.1029/2018GL078582

Zhao, H., Baker, D. N., Li, X., Malaspina, D. M., Jaynes, A. N., and Kanekal, S. G. (2019). On the acceleration mechanism of ultrarelativistic electrons in the center of the outer radiation belt: A statistical study. *J. Geophys. Res.: Space Phys., 124*(11), 8590–8599. https://doi.org/10.1029/2019JA027111

Zhao, Y. W., Xiang, Z., Gu, X. D., Ni, B. B., Ma, X., Lou, Y. Q., Jiao, L. H., Zhou, R. X., Guo, D. Y., … Dong, J. H. (2022). Simultaneous occurrence of four magnetospheric wave modes and the resultant combined scattering effect on radiation belt electrons. *Earth Planet. Phys., 6*(6), 563–575. https://doi.org/10.26464/epp2022050

Zhu, C. B., Zhang, X. G., Zhang, H., Li, X. J., Zong, W. G., Li, J. W., Huang, C., Zhang, C. X., Xiang, Z., … Zhang, X. X. (2022). Inter-calibration between the electron flux measurements of FengYun-3B and Van Allen Probe-A based on electron phase space density conjunctions. *J. Geophys. Res.: Space Phys., 127*(9), e2022JA030463. https://doi.org/10.1029/2022JA030463

Zhu, Q., Cao, X., Gu, X. D., Ni, B. B., Xiang, Z., Fu, S., Summers, D., Hua, M., Lou, Y. Q., … Zhang, W. X. (2021). Empirical loss timescales of slot region electrons due to plasmaspheric hiss based on Van Allen Probes observations. *J. Geophys. Res.: Space Phys., 126*(4), e2020JA029057. https://doi.org/10.1029/2020JA029057

Zong, Q. G., Zhou, X. Z., Wang, Y. F., Li, X., Song, P., Baker, D. N., Fritz, T. A., Daly, P. W., Dunlop, M., … Pedersen, A. (2009). Energetic electron response to ULF waves induced by interplanetary shocks in the outer radiation belt. *J. Geophys. Res.: Space Phys., 114*(A10), A10204. https://doi.org/10.1029/2009JA014393

Zong, Q. G., Yue, C., and Fu, S. Y. (2021). Shock induced strong substorms and super substorms: Preconditions and associated oxygen ion dynamics. *Space Sci. Rev., 217*(2), 33. https://doi.org/10.1007/s11214-021-00806-x